Received: 24 March 2017 | Revised: 1 August 2017 | Accepted: 24 August 2017

DOI: 10.1002/jbio.201700072

Journal of BIOPHOTONICS

FULL ARTICLE

Pixel classification method in optical coherence tomography for tumor segmentation and its complementary usage with OCT microangiography

Alexander Moiseev[1,3]* | Ludmila Snopova[3] | Sergey Kuznetsov[3] | Natalia Buyanova[3] | Vadim Elagin[3] | Marina Sirotkina[3] | Elena Kiseleva[3] | Lev Matveev[2,3] | Vladimir Zaitsev[2,3] | Felix Feldchtein[3] | Elena Zagaynova[3] | Valentin Gelikonov[1,3] | Natalia Gladkova[3] | Alex Vitkin[3,4,5] | Grigory Gelikonov[1,3]

[1]Nano-optics and Highly Sensitive Optical Measurement Department, Institute of Applied Physics Russian Academy of Sciences, Nizhny Novgorod, Russia

[2]Nonlinear Geophysical Processes Department, Russian Academy of Sciences, Nizhny Novgorod, Russia

[3]Laboratory of Optical Coherent Tomography, Nizhny Novgorod State Medical Academy, Nizhny Novgorod, Russia

[4]Departments of Medical Biophysics and Radiation Oncology, University of Toronto, Ontario, Canada

[5]Ontario Cancer Institute, University Health Network, Toronto, Ontario, Canada

***Correspondence**
Alexander Moiseev, Institute of Applied Physics Russian Academy of Sciences, Ulyanova Street 46, 603950 Nizhny Novgorod, Russia.
Email: aleksandr.moiseev@gmail.com

Funding information
Ministry of Education and Science of the Russian Federation (RU), Grant/Award number: 14.B25.31.0015;; Russian Foundation for Basic Research, Grant/Award numbers: 15-42-02513_povolzhie, 16-32-60178 mol_a_dk

A novel machine-learning method to distinguish between tumor and normal tissue in optical coherence tomography (OCT) has been developed. Preclinical murine ear model implanted with mouse colon carcinoma CT-26 was used. Structural-image-based feature sets were defined for each pixel and machine learning classifiers were trained using "ground truth" OCT images manually segmented by comparison with histology. The accuracy of the OCT tumor segmentation method was then quantified by comparing with fluorescence imaging of tumors expressing genetically encoded fluorescent protein KillerRed that clearly delineates tumor borders. Because the resultant 3D tumor/normal structural maps are inherently co-registered with OCT derived maps of tissue microvasculature, the latter can be color coded as belonging to either tumor or normal tissue. Applications to radiomics-based multimodal OCT analysis are envisioned.

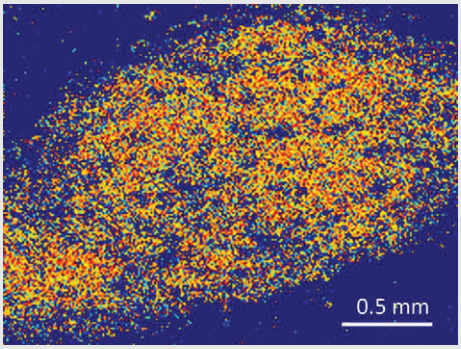

KEYWORDS
image processing, machine-learning, optical coherence tomography

1 | INTRODUCTION

Recent advances in medical image processing, in modalities such as magnetic resonance imaging (MRI) and computed tomography (CT), show that the simultaneous use of many tumor image characteristics may provide additional insights in clinical outcomes prognosis [1–3], prediction of distant metastasis risk [4], and even offer a link to cancer genetics [5]. These methods are known by the common name of radiomics. These features, usually derived from tumor image delineated on MRI or CT, include tumor size and shape features, descriptors of the image intensity histograms, descriptors of the relationships between image voxels (referred to as texture analysis), fractal features, and others. Since all these characteristics are calculated inside tumor regions, their extraction necessitates initial tumor segmentation [1–5].

optical coherence tomography (OCT) is a minimally invasive imaging yielding cross-sectional and volumetric subsurface tissue images with spatial resolution of several

micrometers, to a depth of 1-3 mm [6, 7]. OCT's use in cancer imaging suggests that the radiomics approach can be implemented here as well. In order to do this, one must first develop algorithms for automatically delineating tumors in cross-sectional (2D) and volumetric (3D) OCT images. Further, in developing OCT radiomics, one may use an expanded set of features specific to this modality. That is, in addition to the features commonly used in MRI and CT images analysis, results of various OCT data post-processing yield various other important tissue characteristics such as optical properties [8], polarization metrics [9], biomechanics [10, 11] and microvasculature visualization [12–15]. Among these alternate-contrast-mechanisms OCT approaches, microangiographic visualization seems the most appropriate for use in radiomics, since several quantitative characteristics can be readily extracted. These include vessel tortuosity, distributions of total vessel length, thickness, area or coverage percentage, fractal dimension of the microvascular tree, and others [16, 17]. Some of these characteristics are believed to be correlated with various pathological conditions, including different stages of cancer development [16]. Complementary usage of OCT-based microangiography with structural-image-based tumor classification and/or segmentation will enable such quantification of microvascular networks inside and outside tumor volume separately, thus further increasing the potential number of features which can be used in multi-modal OCT radiomics approach.

In recent years, several OCT classification algorithms have been developed, based primarily on OCT structural images. These utilize various image characteristics, such as intensity, local attenuation coefficient, image textures and so on, and allow classification of morphologically different structures in sites ranging from skin [18] to retina [19] and arterial wall [20]. In this study, an alternate tissue classification based on structural OCT image characteristics was developed, to distinguish between normal and tumor tissue of murine ear implanted with mouse colon carcinoma CT-26 cells. These structural-based classification results were then combined with micro-angiographic maps obtained with M-mode-like speckle variance OCT [14]. Thus, each detected vessel segment was labeled based on whether it passed through the 3D tumor structure as determined from the structural OCT analysis, or alternatively passed through the normal tissue regions surrounding the tumor.

This study was thus comprised of 3 stages: (1) building the classification model based on structural OCT with histological input; (2) resultant model evaluation and independent validation with exogenous-label fluorescence microscopy, and (3) complementary usage of classification model and microangiography results from the same OCT dataset.

Having validated the structural classification approach and quantified its performance, its combination with OCT micro-angiographic data was explored. 3D segmentation of the microvascular maps into "tumor" and "normal" vessels was performed according to their spatial co-localization with the structurally delineated corresponding volumetric tissue regions.

2 | EXPERIMENTAL

2.1 | Animal model

The animal study was approved by the Research Ethics Board of the Nizhny Novgorod State Medical Academy (REB protocol 14, approved December 10, 2013). Thirty BALB/C mice were used. Mouse colon carcinoma CT-26 cells were injected intradermally into the auricle at a dose of 2×105 cells per 20 μL of PBS, as described previously [21]. The tumor grew quite superficially, mostly confined within the epidermis or slightly penetrating it. The resultant tumor structure was clearly visible on OCT in its entirety. Further, the auricle tissue forms well-developed blood flow network, making this preclinical mouse ear + mouse tumor a convenient biological model for multi-modal (microstructural and microvascular) OCT investigations [21, 22].

2.2 | OCT setup and angiography processing

A spectral domain (SD) OCT setup with superluminiscent diode light source at a central wavelength 1300 and 100 nm bandwidth (axial resolution of 10 μm in air) was utilized. Lateral resolution was equal to 15 μm. Scanning system was able to perform 2D lateral scanning, thus providing 3D OCT datasets (2 lateral dimensions plus depth) with an acquisition rate of 20 000 spectral A-scans per second. OCT data for microangiography were acquired from 2×2 mm scanning range, with a dense A-scan pattern of 32 768 A-scans per B-scan. From this data, 3D microvascular network was extracted using high-pass filtering of B-scans via M-mode-like (MML) OCT [14]. Because classification model proposed in this study is intensity based (see below) the actual power of OCT setup was controlled by measuring reflectance from OCT interferometer reference arm and kept constant during the experiments.

2.3 | Expert labeling of OCT tumor images

One hundred and fifty OCT cross-sectional images from 30 animals were labeled by a histopathologist through comparison of OCT and histological images (Figure 1A,B). At this stage of the research, tumor and normal tissue (epidermis, dermis and cartilage) were labeled as "tumor" and "normal" (Figure 1C). Only unambiguous morphological structures were categorized. The expert-labeled images were divided into 2 groups: 100 256×256 pixels cross-sectional

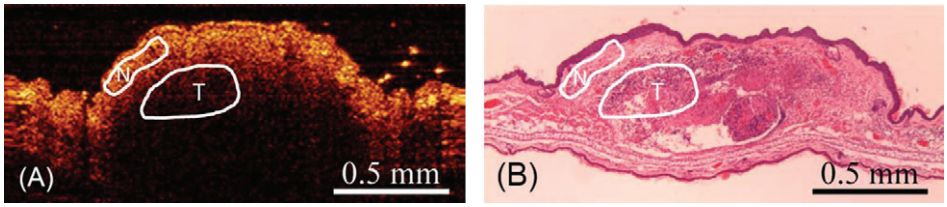

FIGURE 1 Cross-sectional OCT image labeling and tumor/normal tissue segmentation process. A, OCT-image of a CT 26 on ear mice. B, Histology image taken on the same day. Expert labels represent approximately same regions in both images. Area marked with "N" represents "normal" tissue, "T" represents "tumor." Note that only parts of tomograms which display unambiguous morphological structures were labeled by the expert

images from 20 animals were used for classification model training, and 50 images from 10 animal were used for its evaluation. Although these are not large numbers, our analysis is pixel-based and so the data content is significant—every image in the contained ~3000-5000 labeled pixels, thus ~400 000 entries in training set and ~200 000 entries in the evaluation set. The training set was further divided into ~350 000 entries training subset and ~50 000 entries validation set we used to find optimal values for classification method hyperparameters. Images for training and test sets were obtained by downsampling MML OCT B-scans, provided by our setup. B-scans selected for expert evaluation were separated not less than 150 μm from each other. Downsampling and selection of separated images were performed to decrease correlation for training and evaluation datasets between neighboring A-scans and consequently neighboring data-points, thus further increasing information content in the dataset

2.4 | Classification model

To distinguish between normal and tumor tissues of CT-26 in structural OCT images, a supervised classification model was built. The model comprised of 2 major steps: firstly a features set was introduced such that for every pixel in an OCT structural image, a feature vector was defined; secondly, based on these feature vectors, pixel classification was performed. At the learning stage, features were calculated for pixels in the images from training set, and supervised classification method was used to build the classification model. The prediction stage contained an additional stage of image thresholding. Since many pixels in a typical OCT image may represents empty space (eg, above tissue surface or below depth of imaging), these were rejected from the analysis by 2-step operation. In the first step image was hard-thresholded using pre-evaluated average noise level plus triple noise standard deviations as a threshold. Then in the thresholded images isolated connected regions which contains less than 10 pixels were eliminated as well with mathematical morphology operations. The morphology closing operation was then applied to the part of the thresholded image above zero, and only pixels from non-zeros regions of the resulting mask were taken to further analysis. A feature vector was built for every such pixel, and the classification model was applied to these vectors, yielding a resultant label (tumor or normal) only for pixels above the intensity threshold.

The most easily accessible and arguably most information-rich component of an OCT structural image is its signal intensity in each pixel. We thus chose to work with logarithmic values of cross-sectional signal distributions provided by our OCT setup to generate a robust features vector, although the developed methodology can be easily extended to accommodate other aspects of information-rich OCT input data. However even properly handling intensities is challenging, because the signal value in each pixel is defined not only by the optical properties of the corresponding tissue but the optical properties of all tissues above, local light fluence details, and by the speckle noise inherent in OCT. Thus to unambiguously describe local tissue characteristics, brightness of a specific pixel alone is insufficient, and OCT signal distribution in the vicinity of the pixel must be considered. For the "vicinity," we chose 11 pixels above and 12 below the given pixel along the same A-scan (more on this choice below), thus forming an A-scan length window of 24 pixels. The choice of 1 dimensional (A-scan) segment as the "fundamental unit" in the ensuing analysis is logical, as all 2D or 3D OCT images are built up of spatially adjacent A-scans. Instead of using these 24 pixel intensities directly as a features set, we decomposed them into orthogonal basis vectors, and the first 8 coefficients were kept as a features set (more on this choice below). With properly chosen basis vectors set, this step (decomposition and data reduction) can minimize the influence of noisy local intensity changes while keeping/enhancing informational differences between A-scan windows.

To construct the orthogonal basis set, Principal Components Analysis (PCA) was used [23]. This method provides complete set of orthogonal bases (principal components), with the first principal component having the largest possible results variance, the second the second-largest variance and so on. Input for PCA consisted of 1 000 000 randomly selected 24-pixel A-scan windows from about 2000 256 × 256 pixels OCT structural images (20 animals, ~100 images separated by 20 μm per animal). Images were obtained by downsampling MML OCT B-scans, provided by our setup. Downsampling and random selection of data points were performed to ensure absence of correlation

between any 2 vectors from this auxiliary dataset. Resultant set of principal components (as mentioned we retained 8) was used to build features vectors for the classification model below.

A popular state-of-the-art method of random forest trees classification was chosen [24]. At the learning stage, this method takes a set of feature vectors as input and corresponding set of outputs (expert labels in our case), and builds a set of decision-trees classifiers. While building each particular decision tree, the algorithm picks a random subset of input vectors and random subset of the features vectors. This random picking approach avoids the common decision trees problem of overfitting [24]. At the prediction stage, the algorithm takes an input vector and applies all built decisions trees to it. The vector gets the label (tumor or normal in our case) which is predicted by the majority of the trees composing the classifier. The part of the decision trees giving the particular label for the features vector can be considered as a probability of this vector to have that particular label [24]. In this study, such value for "tumor" label was used as a probability of a given pixel to represent a tumor, ranging for 0 to 1. The overview our OCT feature building and classification processes is displayed in Figure 2. Note that as all processing is A-scan based and SD OCT system records A-scans independently, the whole processing does not depend on system scanning range. Because classification model proposed in this study is intensity based, in order to apply the classification model trained on dataset obtained from one OCT setup to the dataset obtained on another OCT setup, the additional preprocessing step matching intensity histograms of both datasets should be performed.

2.5 | Classification model hyperparameters adjustment

The proposed classification method has 2 types of hyperparameters. Firstly, the feature vector parameters such as A-scan window length and number of retained coefficients

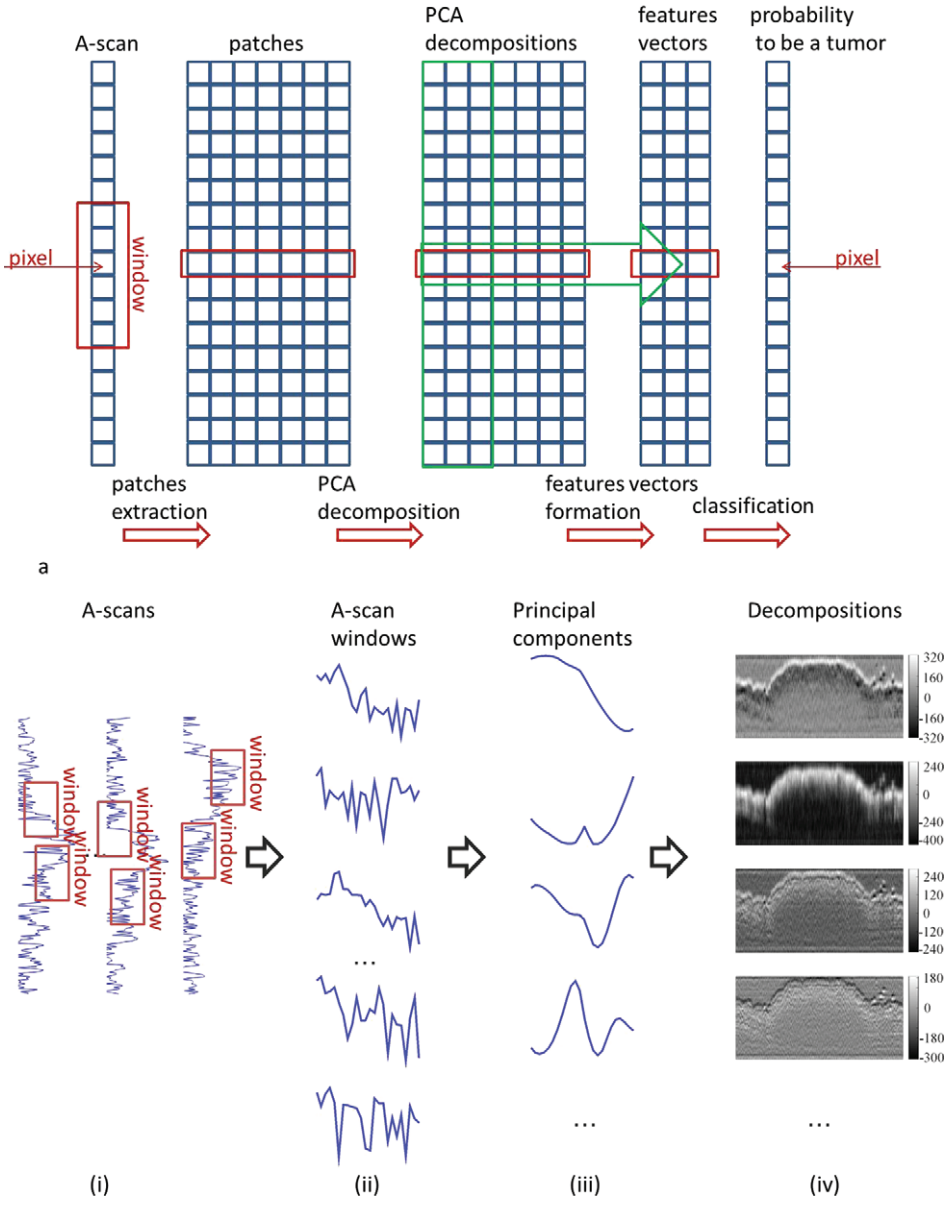

FIGURE 2 A, Overview of feature calculation process, from "pixel" in the A-scan to its predicted probability to be a tumor. Red box represents modification of a window corresponding to a pixel of interest (marked with arrow and subscribed). Green box and arrow represent part of PCA decomposition coefficient used as a feature vector. A-scan window and features vector sizes are schematically shown to be 7 and 3 U (for diagrammatic convenience); the actual values used values used in the analysis were 24 and 8, respectively. B, An illustration of feature vector construction process; (i) schematics of typical A-scans showing typical A-scan analysis windows; (ii) several examples of A-scan windows of length 24 pixels; (iii) first 4 principal components from PCA; (iv) decomposition of the tomogram into these 4 components. Coefficients of such decompositions (of the first 8 principal components) were used as a features vector in the developed classification model

from A-scan window principal components decomposition. Secondly, classification model (ie, random forest classifier) parameters such as number of decision trees in the forest, the number of features to consider when looking for the best split, the maximum depth of the decision tree, the minimum number of samples required to split an internal node of the tree, the minimum number of samples required to be at a decision tree leaf node. To find the optimal set of these parameters we evaluate the performance of the model trained on the training subset on the validation subset using area under receiver operating characteristic (ROC) curve [25] as a metric. First we set classification model parameters to be 10 decision trees with unlimited depth which use 3 randomly selected features from the feature vector and minimum number of samples required to split an internal node of the tree and minimum number of samples required to be at a decision tree leaf node both equal to 1. Then we consequentially tuned A-scan window length and number of retained coefficients from A-scan window principal components decomposition one after another while holding the second parameter constant. After first estimation for feature vector parameters were found, we tuned classification model parameters in the same fashion. Then we repeated the process for feature vector parameters using adjusted classification model parameters. The process was repeated until no improvements were made by independently tuning single model parameter. The resulting set of the hyperparameters was: A-scan window length is equal to 24, number of retained coefficients from A-scan window principal components decomposition is equal to 8, number of decision trees in the forest is equal to 11, the number of features to consider when looking for the best split is equal to 3, the maximum depth of the decision tree is equal to 8, the minimum number of samples required to split an internal node of the tree is equal to 17, the minimum number of samples required to be at a decision tree leaf node is equal to 8.

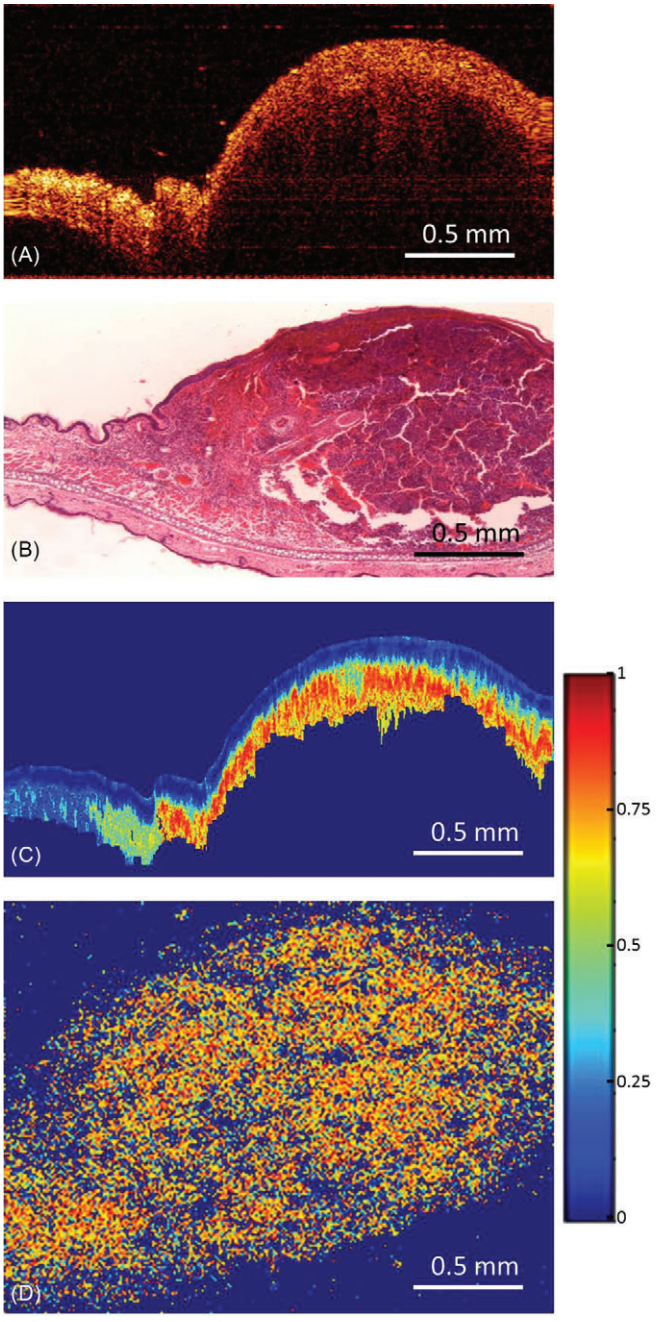

FIGURE 3 Cross-sectional OCT images pixel classification process. A, OCT-image of a CT 26 on ear mice, (B) correlated histology, (C) Prediction of classification algorithm: Map of tumor probability; (D) En face projection of the tumor region as described in Section 2.6. Values in (B) and (C) from 0 to 1, as per color-bar

2.6 | Tumor en face projection

For display convenience, en face projection of classification results were also introduced (note that this is different from "conventional" C-scan en face structural OCT displays). The standard in OCT-based microangiography maximum intensity projection (MIP) is not applicable in this case, as every single misclassified pixel in A-scan will display the whole A-scan as a "tumor" in MIP. Thus the modification of other popular choice in 2D projection of 3D vessel network was chosen: the mean intensity projection. The mean was taken after signal thresholding from probability-to-be-a-tumor value from along every A-scan. In the current study this distribution is referred as "tumor en face projection" (Figure 3C).

2.7 | Classification model evaluation

After classification model was built as per Section 2.4, 2.5 it was applied to the expert-labeled images from animals which were not involved in the model learning stage and tumor classification labels made by histopathologist who examined both OCT and histological images were compared with the probability of these pixels to be a tumor as predicted by the proposed algorithm. As a metric of classifier performance, area under ROC curve [25] was used.

2.8 | Independent technique validation—comparison with fluorescence

Since experts labeled only those regions of OCT images which they reliably identified as normal or tumor tissues, transition zones were problematic because no unequivocal expert labeling is possible there. Thus the performance of the classifier on the borders of pathology requires additional evaluation. To enable this, a mouse with genetically encoded fluorescent protein KillerRed, expressed by CT-26 murine colon carcinoma, was imaged using both fluorescence microscopy and OCT. Both images were acquired at 14th day after tumor cells inoculation. Every cross-sectional structural OCT image, forming 3D OCT dataset, was processed with proposed algorithm. Since the fluorescence microscope used in this study is only capable of 2D depth integrated image acquisition, visible classifier borders of the tumor on the 2D en-face OCT projection (according to Section 2.6) were compared with KillerRed fluorescence images.

To increase OCT field of view, 2 consecutive OCT spatially overlapping datasets were acquired and aligned using OCT-based angiography images.

Tumor borders in both modalities (fluorescence and classified OCT volumetric dataset) were obtained by splitting pixels in corresponding images in 2 clusters according to their values (intensity in case of fluorescence image and probability-to-be-a-tumor projection in case of OCT image) using *k*-means algorithm [26]. The borders of the cluster with higher average value were treated as tumor borders.

Aligning of en face OCT and fluorescence images was done by superimposing vessels meshworks, visible in both modalities. For blood vessels visualization with fluorescence, a fluorescein isothiocyanate (FITC) conjugated with 150 kDa Dextran was used and. Both KillerRed and FITC fluorescence were imaged on the same microscope (Axio Zoom V16, Zeiss, Germany) with the same position of the tissue, by changing respective filter sets.

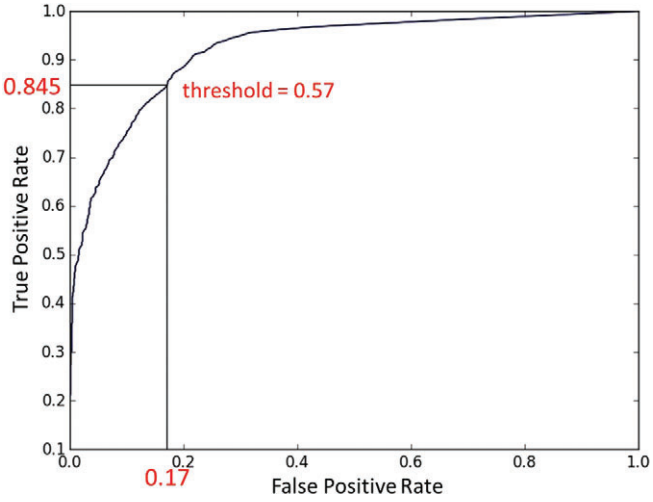

FIGURE 4 ROC curve for proposed pixel classification method (area under curve equal to 0.93). For probability of a pixel to be a tumor value threshold 0.57 providing sensitivity equal to 0.84 and specificity equal to 0.83 was chosen for 3D tumor delineation

3 | RESULTS AND DISCUSSION

3.1 | Classification model evaluation

In Figure 4 ROC curve for the obtained classification results vs expert labels for the test data is shown. ROC illustrates the performance of a classifier as its discrimination threshold (probability of pixels to be a tumor in the case of present study) is varied. The curve is created by plotting the true positive rate against the false positive rate at various threshold settings. For the described tumor vs normal tissue classifier, the area under the ROC was equal to 0.93. This encouragingly high number can potentially be improved further if we account for "co-localization," that is the tendency of similarly labeled pixels to cluster together or use additional OCT image modalities (eg, attenuation coefficient distribution, OCT image in cross-polarization, etc.) for feature construction.

Analysis of the ROC curve allows selection of the "optimal" threshold value for the continuous classification result in order to build binary classification, that is value providing balance between classification model sensitivity and specificity. For the obtained classification threshold value was chosen equal to 0.57, which provides binary classification sensitivity equal to 0.84 and specificity equal to 0.83 (see Figure 4). This "optimal" value was further used for tumor border delineation.

As seen from Figures 3C, 6E,F, the majority of false positive classifications were originated from lower intensity regions. This is the consequence of the fact that in lower intensity regions signal-to-noise ratio is lower and classification outcome is largely affected by noise.

3.2 | Independent technique validation—comparison with fluorescence

For independent technique validation en-face borders, of the tumors obtained according to Section 2.6 from 3D volumetric classification results were superimposed with fluorescence image of CT-26 murine colon carcinoma expressed genetically encoded fluorescent protein KillerRed. The results are shown in figure.

It should be pointed out, that the comparison of volumetric images obtained in both modalities would provide less ambiguous results. However selected animal model does not allow imaging of the tumor with scanning confocal microscopy available for the authors since its imaging depth does not allow imaging below the skin. Thus comparison of 2D images obtained with fluorescence microscopy and OCT

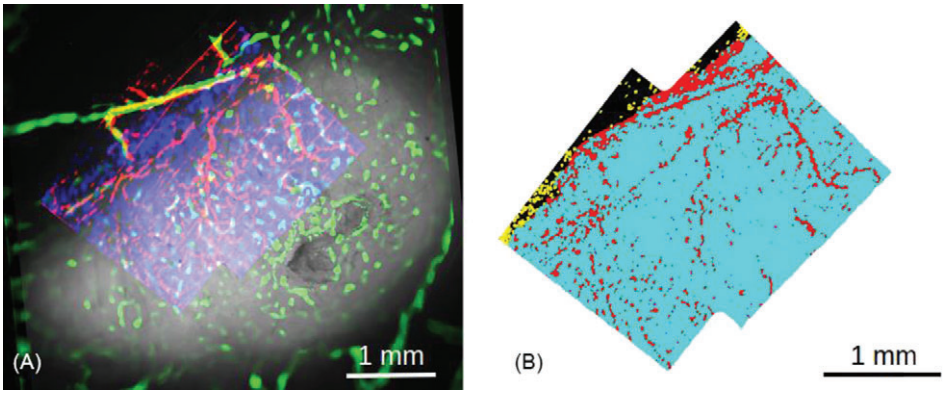

FIGURE 5 A, Alignment of fluorescence and OCT and fluorescence images by superimposing vessels meshworks (green—vessels visible in fluorescence, red—vessels obtained by OCT angiography processing). In purple en face projection of OCT classification results is presented, tumor visible in fluorescence channel is presented in gray. B, Overlapping of tumor projections visible in fluorescence and obtained by the proposed OCT pixel classification method. Having fluorescence image as a ground truth cyan represented true positive classification, red—false negative and yellow—false positive. See text (Section 2.8) for tumor images binarization details. Note that some of the false negative pixels inside the tumor margins follow the large vessels. These false negative classifications are result of shadowing of the tumor in the OCT images by shadows below the large vessels above the tumor. As these shadowed regions were below intensity threshold, they were excluded from the classification thus providing false negative pixels in en-face projection

classification en face projection was chosen for proposed classification technique validation. One should keep in mind that different imaging depth for both modalities and different position of the object relative to imaging device will lead to border mismatch that does not evaluate classification performance, thus both factors should be taken into account in interpretation of the results. Since position of the object relative to imaging device will affect angiography image as well, the ability to overlay vessels projections, obtained using OCT angiography and using fluorescence imaging using only translation rotation and scaling will guarantee conformity of the objects positions in both modalities which was the case in the present experiment (see Figure 5A). Equality of imaging depths was ensured by chosen model, since imaging depth was primarily defined by ear thickness.

3.3 | Complementary usage of OCT angiography and structural image classification

During tumor growth, intricate and complex microvasculature is seen to develop and can be accurately visualized with MML-OCT technique in 3D [21]. Combining these microvascular maps with microstructural tissue classification results can potentially provide more insights into the normal-pathology transformations of the cellular and microvascular tissue compartments, and their spatial inter-relationships. We thus proceeded to label the microvascular network as spatially overlapping in 3D with tumor or with surrounding normal tissue.

To enable accurate co-usage of labeled OCT structural maps with OCT angiography, the microvascular networks from the latter were first binarized in 3D. Then each binarized vessel, intersecting with an area where the probability of a voxel belonging to a tumor exceeded the threshold defined in Section 3.1 was marked as "vessel inside tumor region"; otherwise it was marked as "vessel inside normal region." The probability threshold value was chosen to provide balance between sensitivity and specificity of the proposed classification method. The resultant color-coded 3D results are presented in Figure 5C,D. Note the interesting difference that this analysis reveals—otherwise similar-looking microvascular maps of 2 different tumor networks (Figure 5A,B) now show many more "tumor" vessels in the second case compared to the first.

All vessels were skeletonized and their total length was calculated. Quantifying this newly revealed information, we calculate similar overall vessel length for the 2 cases (difference between 2 cases was equal to 1.3%), but significant difference in the "tumor compartment" vessel length (difference between 2 cases was equal to −40%). Further analysis of the 2 microvascular networks ("normal" and "tumor"), across and within different animal images, will quantify the metrics of vessel thickness, volumetric density, tortuosity, fractal dimension and so on. The resultant numbers be used as additional information-rich input data to derive advanced features vectors for OCT radiomics.

4 | CONCLUSION

The proposed tumor classification method provides reliable results for segmenting tumor regions from normal tissues on

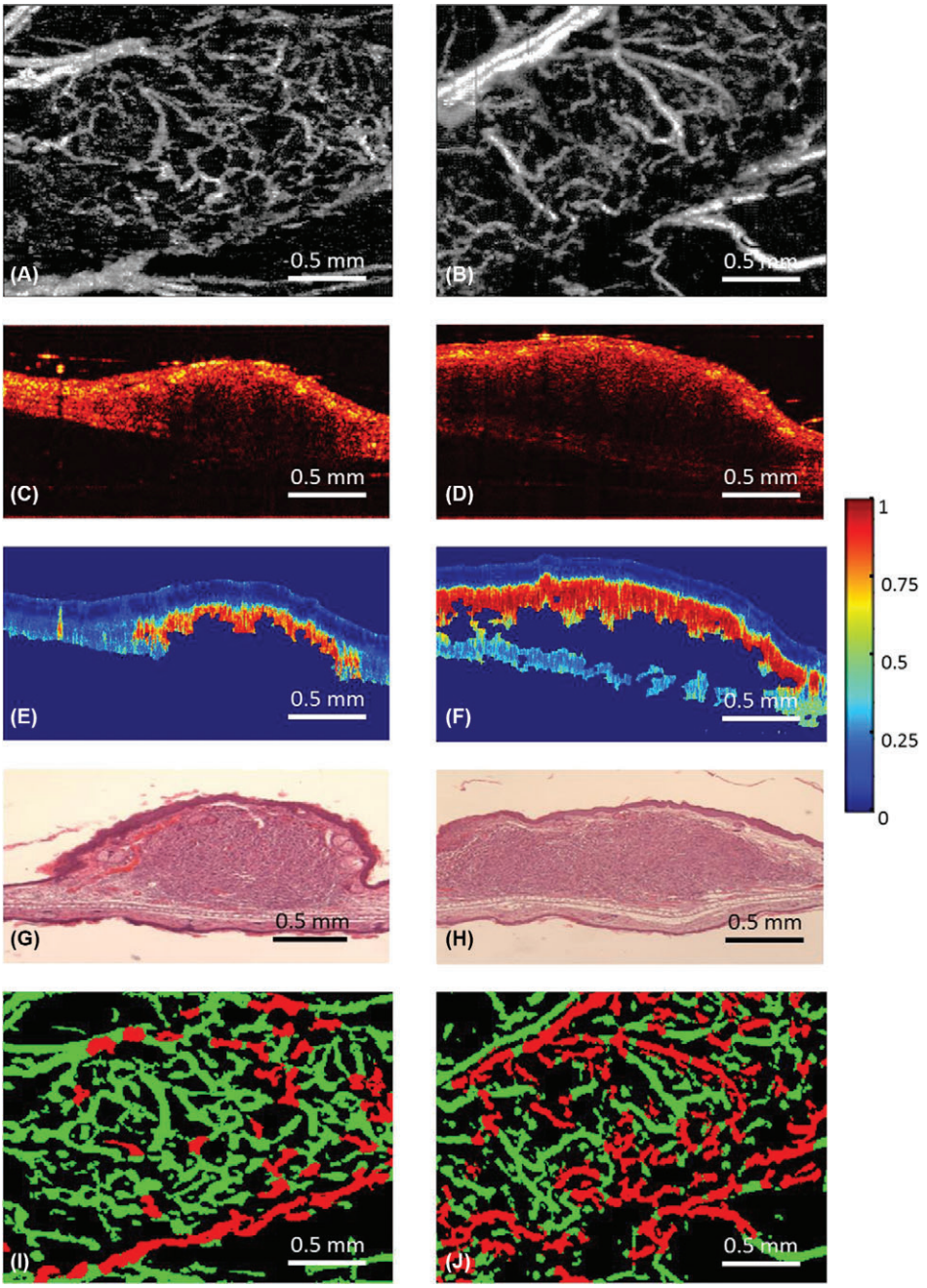

FIGURE 6 Complementary usage of OCT angiography and structural tumor/normal tissue classification. A and B, MML-OCT MIP microvascular images from 2 different CT-26 colon tumors growing in a mouse ear. Note the similar visual appearance of the 2 resultant microvascular networks. C and D, Cross-sectional images from the OCT volume used to construct microvasculature images from (A,B). E,F, Classification results of C,D. Note the misclassification of the vessels shadow in E. This shadow had not been excluded from the analysis in thresholding step leading to the misclassification. G and H, Correlated histology for (E,F). I and J, Same images as from (A,B) but now color-coded as co-localized within structurally-segmented tumor tissue (red) or within normal tissue (green). Note that the second tumor is seen to contain many more "tumor" vessels compared to the first (difference of 40%, as discussed in the text)

OCT structural images. For probability-to-be-a-tumor value specificity and sensitivity of 0.84 and 0.83, respectively, can be reached. These promising values of specificity and sensitivity will enable one to calculate OCT image statistics inside and outside tumors (eg, intensity histogram characteristics, image texture metrics and other structural image features of potential interest to the emerging OCT radiomics approaches). Complementary usage of classification results with OCT-derived and co-registered microvascular maps similarly allows calculation of numerical characteristics of vasculature networks inside and outside tumor regions separately. These may be used to study differences between different microvascular networks otherwise similar in appearance, and to further enhance the quantifiable data content of multimodal OCT for radiomics-like analysis.

In addition to using the microvascular data with the microstructural classification results as demonstrated, complimentary OCT information (eg, polarimetric and elastographic metrics) can be straightforwardly introduced into the proposed framework as well. By calculating the proposed feature vector for each OCT contrast modality and combining, an enhanced feature vector can be constructed and introduced into the model learning and predicting processes. This may have relevance in the emerging field of radiomics as applied to OCT.

ACKNOWLEDGMENTS

The biological part of this work as well as the development of the MML-OCT equipment were supported by the

Ministry of Education and Science of the Russian Federation, grant no. 14.B25.31.0015; optimization of the angiographic processing was supported by RFBR grant no. 15-42-02513_povolzhie; development of OCT images classification technique as well as OCT angiography image post-processing and enhancement were funded by RFBR project no. 16-32-60178 mol_a_dk

REFERENCES

[1] P. Lambin, E. Rios-Velazquez, R. Leijenaar, S. Carvalho, R. G. van Stiphout, P. Granton, C. M. Zegers, R. Gillies, R. Boellard, A. Dekker, *Eur. J. Cancer* **2012**, *48*, 441.
[2] C. Parmar, R. T. Leijenaar, P. Grossmann, E. R. Velazquez, J. Bussink, D. Rietveld, M. M. Rietbergen, B. Haibe-Kains, P. Lambin, H. J. Aerts, *Sci. Rep.* **2015**, *5*, 11044.
[3] E. R. Velazquez, C. Parmar, M. Jermoumi, R. H. Mak, A. van Baardwijk, F. M. Fennessy, J. H. Lewis, D. De Ruysscher, R. Kikinis, P. Lambin, *Sci. Rep.* **2013**, *3*, 3529.
[4] T. P. Coroller, P. Grossmann, Y. Hou, E. R. Velazquez, R. T. Leijenaar, G. Hermann, P. Lambin, B. Haibe-Kains, R. H. Mak, H. J. Aerts, *Radiother. Oncol.* **2015**, *114*, 345.
[5] D. A. Gutman, W. D. Dunn Jr.. , P. Grossmann, L. A. Cooper, C. A. Holder, K. L. Ligon, B. M. Alexander, H. J. Aerts, *Neuroradiology* **2015**, *57*, 1227.
[6] A. F. Fercher, C. K. Hitzenberger, G. Kamp, S. Y. El-Zaiat, *Opt. Commun.* **1995**, *117*, 43.
[7] D. Huang, E. A. Swanson, C. P. Lin, J. S. Schuman, W. G. Stinson, W. Chang, M. R. Hee, T. Flotte, K. Gregory, C. A. Puliafito, *Science* **1991**, *254*, 1178.
[8] D. J. Faber, F. J. Van der Meer, M. C. Aalders, T. G. van Leeuwen, *Opt. Express* **2004**, *12*, 4353.
[9] M. Pircher, E. Goetzinger, R. Leitgeb, C. Hitzenberger, *Opt. Express* **2004**, *12*, 3236.
[10] B. F. Kennedy, K. M. Kennedy, D. D. Sampson, *IEEE J. Sel. Top. Quant. Electron.* **2014**, *20*, 272.
[11] V. Y. Zaitsev, I. Vitkin, L. Matveev, V. Gelikonov, A. Matveyev, G. Gelikonov, *Radiophys. Quant. Electron.* **2014**, *57*, 210.
[12] Z. Chen, T. E. Milner, D. Dave, J. S. Nelson, *Opt. Lett.* **1997**, *22*, 64.
[13] A. Mariampillai, B. A. Standish, E. H. Moriyama, M. Khurana, N. R. Munce, M. K. Leung, J. Jiang, A. Cable, B. C. Wilson, I. A. Vitkin, *Opt. Lett.* **2008**, *33*, 1530.
[14] L. A. Matveev, V. Y. Zaitsev, G. V. Gelikonov, A. L. Matveyev, A. A. Moiseev, S. Y. Ksenofontov, V. M. Gelikonov, M. A. Sirotkina, N. D. Gladkova, V. Demidov, *Opt. Lett.* **2015**, *40*, 1472.
[15] R. K. Wang, S. L. Jacques, Z. Ma, S. Hurst, S. R. Hanson, A. Gruber, *Opt. Express* **2007**, *15*, 4083.
[16] L. Conroy, R. S. DaCosta, I. A. Vitkin, *Opt. Lett.* **2012**, *37*, 3180.
[17] R. Reif, J. Qin, L. An, Z. Zhi, S. Dziennis, R. Wang, *J. Biomed. Imag.* **2012**, *2012*, 9.
[18] D. Sheet, A. Chaudhary, S. P. K. Karri, D. Das, A. Katouzian, P. Banerjee, N. Navab, J. Chatterjee, A. K. Ray, *J. Biomed. Opt.* **2013**, *18*.
[19] K. Vermeer, J. Van der Schoot, H. Lemij, J. De Boer, *Biomed. Opt. Express* **2011**, *2*, 1743.
[20] Y. Gan, D. Tsay, S. B. Amir, C. C. Marboe, C. P. Hendon, *J. Biomed. Opt.* **2016**, *21*.
[21] N. Gladkova, M. Sirotkina, N. Buyanova, T. Kalganova, M. Karabut, V. Elagin, S. Kuznetsov, L. Snopova, G. Gelikonov, V. Y. Zaitsev. *Sovremennye Tehnologii v Medicine*. **2015**, *7*.
[22] Y. Jung, S. Dziennis, Z. Zhi, R. Reif, Y. Zheng, R. K. Wang, *PLoS One* **2013**, *8*, e57976.
[23] G. H. Dunteman, *Principal Components Analysis*, Sage, Newbury Park, CA, **1989**.
[24] L. Breiman, *Mach. Learn.* **2001**, *45*, 5.
[25] J. A. Hanley, B. J. McNeil, *Radiology* **1982**, *143*, 29.
[26] J. A. Hartigan, *J. R. Stat. Soc. Ser. C. Appl. Stat.* **1979**, *28*, 100.

How to cite this article: Moiseev A, Snopova L, Kuznetsov S, et al. Pixel classification method in optical coherence tomography for tumor segmentation and its complementary usage with OCT microangiography. *J. Biophotonics*. 2018;11:e201700072. https://doi.org/10.1002/jbio.201700072